nanomaterials

MDPI

Article

Heat Treatment and Dynamic Mechanical Analysis Strain Sweep Effects on the Phase Structure and Morphology of an Fe-28Mn-6Si-5Cr Shape Memory Alloy

Mihai Popa [1], Florin Popa [2], Bogdan Pricop [1], Nicanor Cimpoeșu [1], Nicoleta-Monica Lohan [1], Gabriel Kicsi [1], Bogdan Istrate [3] and Leandru-Gheorghe Bujoreanu [1,*]

[1] Faculty of Materials Science and Engineering, "Gheorghe Asachi" Technical University of Iași, Blvd. Dimitrie Mangeron 71A, 700050 Iași, Romania; bogdan.pricop@academic.tuiasi.ro (B.P.)
[2] Faculty of Materials and Environmental Engineering, Technical University from Cluj-Napoca, Blvd. Muncii, No. 103-105, 400641 Cluj-Napoca, Romania
[3] Faculty of Mechanical Engineering, "Gheorghe Asachi" Technical University of Iasi-Romania, Blvd. Dimitrie Mangeron, No. 61-63, 700050 Iași, Romania
* Correspondence: leandru-gheorghe.bujoreanu@academic.tuiasi.ro; Tel.: +40-727-486-406

Abstract: Fe-Mn-Si-based shape memory alloys (SMAs) have been extensively investigated since 1982 for various useful properties that enhance the development of different applications such as anti-seismic dampers for very tall buildings, pipe joints, or rail fasteners. In particular, the Fe-28Mn-6Si-5Cr (mass. %) alloy has been mainly used in vibration mitigation or self-adjustable axial displacement applications. Dynamic mechanical analysis (DMA), performed by strain sweeps (SS), enables the monitoring of the evolution of storage modulus and internal friction variations with increasing strain amplitudes at different constant frequencies and temperatures. Thus, applying dynamic bending with various frequencies and amplitudes that actually represents an isothermal mechanical treatment. In the present paper, an Fe-28Mn-6 Si-5Cr (mass. %) SMA was cast by ingot metallurgy, hot-rolled, and water quenched in order to obtain thermally induced martensite and avoid the occurrence of cooling cracks. The influence of the holding time, between 2 and 10 h, at 1050 °C and the effects of DMA-SS performed at three different frequencies were analyzed by a differential scanning calorimetry, an X-ray diffraction, and a scanning electron and atomic force microscopy. The effects of the holding time and mechanical treatment on the structure and morphology of martensite plates were corroborated with the results of the thermal analysis.

Keywords: dynamic mechanical analysis; internal friction; storage modulus; differential scanning calorimetry; precipitation; shape memory alloy; martensite plates

check for updates

Citation: Popa, M.; Popa, F.; Pricop, B.; Cimpoeșu, N.; Lohan, N.-M.; Kicsi, G.; Istrate, B.; Bujoreanu, L.-G. Heat Treatment and Dynamic Mechanical Analysis Strain Sweep Effects on the Phase Structure and Morphology of an Fe-28Mn-6Si-5Cr Shape Memory Alloy. *Nanomaterials* **2023**, *13*, 1250. https://doi.org/10.3390/nano13071250

Academic Editor: Jürgen Eckert

Received: 7 March 2023
Revised: 28 March 2023
Accepted: 30 March 2023
Published: 1 April 2023

1. Introduction

Fe-Mn-Si shape memory alloys (SMAs) have been extensively investigated in the last four decades due to their lower cost compared to NiTi-based SMAs [1], their superior mechanical properties, such as high recovery stresses, good machinability, weldability, or formability [2], and their fair corrosion resistance [3]. It has been pointed out that small Si additions to Fe-30Mn alloys (in mass. %, as all chemical compositions will be given hereinafter) promote a reversible martensitic transformation [4]. Thus, ε-hexagonal close-packed (hcp) stress-induced martensite retransforms to γ-face-centered cubic (fcc) austenite during heating, and this is the mechanism of the shape memory effect (SME) in Fe-Mn-Si SMAs [5]. The occurrence of α′ (body-centered cubic, bcc) martensite, observed at low Mn amounts or high deformation degrees, mostly in the intersection areas of ε-hcp martensite plates, delays the reverse martensitic transformation [6]. Aiming to increase the corrosion resistance, Cr was added, and, thus, Fe-28Mn-6Si-5Cr SMA was developed [7], which became of practical use for the construction of steel pipe couplings for fluid transport [8] or pipe joining in tunnel making [9], crane rail fasteners [10], and concrete reinforcing bars [11]. The feasibility of truncated cone modules being used for the self-adjustable axial loading of angular contact bearings, such as to restore the contact between balls and cage, was demonstrated [12]. In particular, Fe-28Mn-6Si-5Cr SMA has been mainly used in vibration mitigation applications [13], as it belongs to inter-phase boundary-type high-damping materials, in which internal friction (IF) is caused by the hysteretic movement of the interfaces during the stress-induced martensitic transformations [14]. Since both SME and IF are based on the reverse movement of the γ/ε interface [5], the relationship between these two phenomena and the stress-induced formation of ε-hcp martensite from γ-fcc austenite has been intensely studied in Fe-Mn-based SMAs [15]. Considering the necessity to accurately evaluate the elastic–plastic behavior and energy dissipation capacity of a given material, dynamic mechanical analysis (DMA) has been developed as a measuring technique for transformation temperatures of solid state transitions, storage modulus (E′), loss modulus (E″), and IF ($\tan\delta = E''/E'$) [16]. This technique comprises the dynamic loading of a specimen, performed during heating–cooling (temperature scans, TS) or isothermal strain sweeps (SS), with controlled force, deformation, frequency, and temperature. Various specimen holders may be used, among which three-point-bending (3PB) is one of the most popular [17].

Some previous studies on manganese (Hadfield) steel have reported that the DMA strain sweeps that are performed with a three-point-bending specimen holder (DMA-SS-3PB) are able to influence the microstructure that causes the formation of parallel arrays of micro-slip bands with submicronic spacing [18] and the preferred reordering tendency of carbon atoms [19]. On the other hand, DMA has been widely used as a measuring technique for the viscoelastic and damping properties of Fe-Mn-Si-based SMAs [20], while for Fe-28Mn-6Si-5Cr SMA, a strong influence of thermomechanical treatments on the IF values was reported [21]. Based on these results, the present authors focused their attention on Fe-28Mn-6Si-5Cr SMA and observed that, besides thermomechanical treatments, the IF values are also influenced by the dynamic deformation frequency [22]. Moreover, it has been demonstrated that DMA-SS-3PB, itself can be considered a mechanical treatment, since the storage modulus increases and saturates due to work hardening, while the IF experiences a local maximum [23].

The present paper aims to analyze the cumulative effects of the heat treatments, quantified by maintaining periods during the solution treatment, and the dynamic bending frequency, during DMA-SS-3PB, on the structure of an Fe-28Mn-6Si-5Cr SMA.

2. Materials and Methods

An Fe-28Mn-6Si-5Cr alloy was melted from high-purity elemental powders (over 99%) provided by Sigma Aldrich Merck (Darmstadt, Germany) in a FIVE CELLS levitation induction furnace (Lautenbach, France) and cast into water-chilled copper molds. From machined ingots, with typical dimensions of ϕ 20 × 45 mm, fragments were longitudinally cut and hot-rolled (1050 °C) until their thickness decreased to 1 mm. Further thickness reduction was achieved by intensive polishing under water cooling until reaching a 0.7 mm thickness. Rectangular specimens (0.7 × 4 × 25 mm) were cut on a wire spark erosion machine. The gradual change in the shape of manufactured specimens is illustrated in Figure S1 from Supplementary Material. Twenty-five samples were solution-treated at 1050 °C, a temperature that was used for the homogenization of this alloy [24]. During the solution treatment, every five samples were maintained for five different time durations: 2, 4, 6, 8, and 10 h, respectively, with final water quenching.

By means of a Setaram Labsys calorimeter (Setaram, Caluire, France), differential scanning calorimetry (DSC) tests were performed using small fragments, weighing less than 50 mg, and cut with a low-speed saw from the five solution-treated states. DSC charts were recorded both during heating, with a rate of 10 °C/min, up to 1050 °C, and during subsequent isothermal holding for 10 h.

Three samples of each of the above-mentioned five solution-treated states underwent DMA-SS-3PB by means of an analyzer-type DMA 242 Artemis NETZSCH (Netzsch, Selb, Germany), with force resolution of 0.0005 N, amplitude range: ±0.1 up to 240 μm, and amplitude resolution of 0.0005. Each of the three specimens was subjected to five consecutive cycles of strain sweep at room temperature (RT), with different frequencies: 1, 5, and 10 Hz, respectively, during which strain amplitude increased between 0.01 and 0.08%. Hereinafter, the specimens will be designated by their respective holding times and DMA-SS frequency (e.g., 2 h–1 Hz, 10 h–10 Hz). Considering that the first cycle usually corresponds to a transient phenomenon, it was removed from the diagrams, and the average values of E′ and tanδ were calculated from the second to the fifth cycle by means of PROTEUS software (v.6.1, Selb, Germany) that the DMA device is equipped with.

The structural effects of these treatments were evaluated by X-ray diffraction (XRD), scanning electron and atomic force microscopy (SEM and AFM).

XRD used an Expert PRO MPD diffractometer (Malvern Panalytical B.V., Almelo, Netherlands) with Cu Kα radiation. XRD patterns were recorded in the significance region 2θ = 40–100°. XRD maxima identification of γ-fcc, ε-hcp and α′-bcc phases was conducted using crystallographic databases and 01-071-8288, 01-071-8285, and 00-034-0396 JCPDS files, respectively. SEM micrographs were recorded on polished and etched surfaces with a JEOL JSM-5600LV device, which was equipped with an Oxford Instruments EDX (energy dispersive X-ray spectrometry) detector (INCA 200 software).

AFM micrographs were recorded with NanoSurf (Liestal, Switzerland) easyScan 2 equipment on electropolished surfaces. The morphologic particularities of martensite plates were investigated and measured, as previously pointed out [25].

3. Results

3.1. DSC Evaluation

Figure 1 separately summarizes the heat flow variations during the first two steps of the solution treatment: heating and holding.

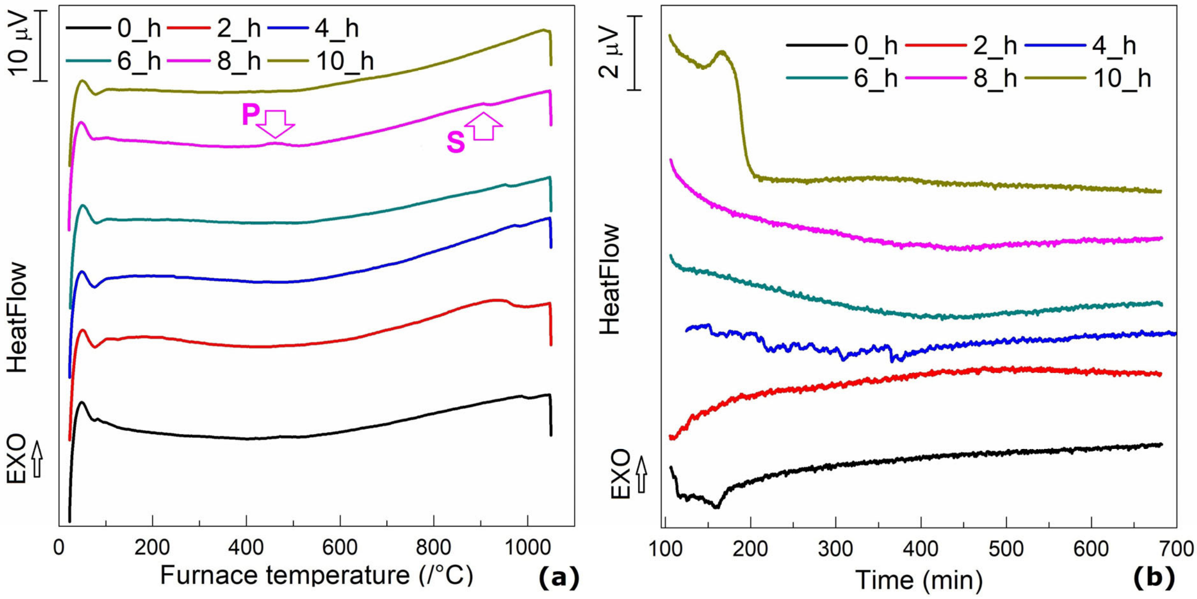

Figure 1. DSC thermograms emphasizing heat flow variations during the first two steps of solution treatment: (**a**) heating up to 1050 °C and (**b**) 10 h of holding at 1050 °C. P: precipitation; S: solvus.

On the DSC thermograms recorded during the heating of fragments cut from solution-treated specimens, Figure 1a revealed an exothermic peak located around 500 °C at the specimens solution treated for 8 and 10 h [23]. In the present case, due to the representation at the same temperature scale, the exothermic maximum is more obvious in the specimen solutions treated for 8 h. These peaks can be ascribed to a precipitation phenomenon. In addition, most of the DSC charts revealed an endothermic step, located around 900–950 °C, which corresponds to the solvus line [26]. It is noticeable from Figure 1b that the solution treatment's holding time altered the heat flow variation during holding. The heat flow had an increasing tendency in time at specimens in the initial condition and solution-treated for 2 h, remained almost constant at the specimen held for 4 h, and experienced a decreasing tendency at specimens maintained for 6, 8, and 10 h.

3.2. DMA Evaluation

Figure 2 illustrates the variations in average values of E′ and tanδ with a strain amplitude for nine of the fifteen specimens under study.

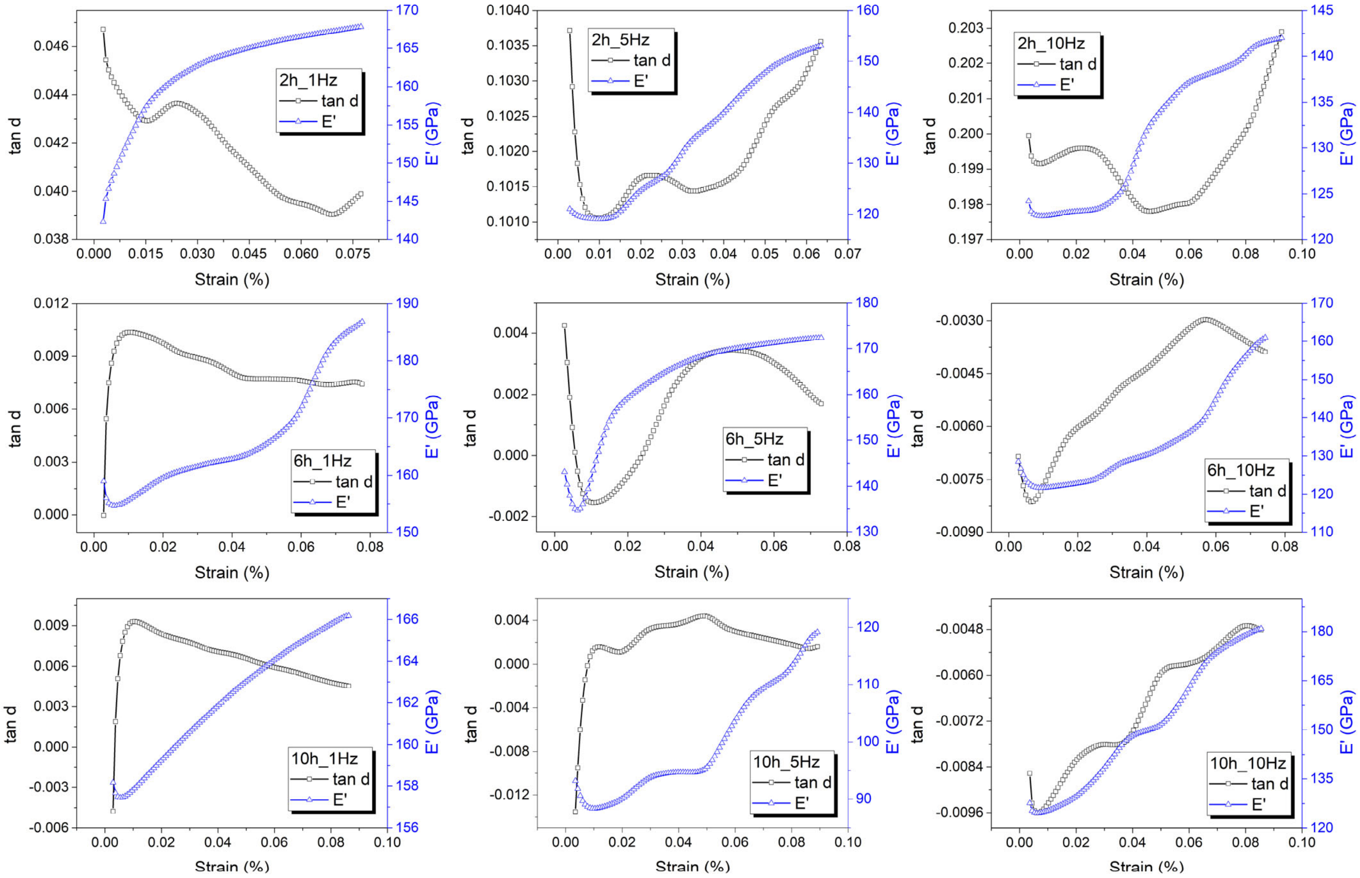

Figure 2. Variations of the average values of E′ and tanδ with strain amplitude as a function of holding time (2, 6, and 10 h, from **left** to **right**) and strain sweep frequency (1, 5, and 10 Hz, from **top** to **bottom**).

In all of the diagrams, the storage modulus (E′) increased up to saturation, which was an effect of work hardening [23]. All the tanδ variations present a maximum that tends to increase with the DMA-SS-3PB frequency only for the specimens that were solution-treated for short holding times (2 h), and the same aspect was observed for the specimens solution-treated for 4 h. For longer holding times, it is expected that the precipitates might produce a "pinning effect" that blocks interface displacement [27].

3.3. SEM Investigations

The characteristic SEM micrographs of the specimens in initial hot-rolled condition and after solution treatment, prior to DMA-SS-3PB, are summarized in Figure 3.

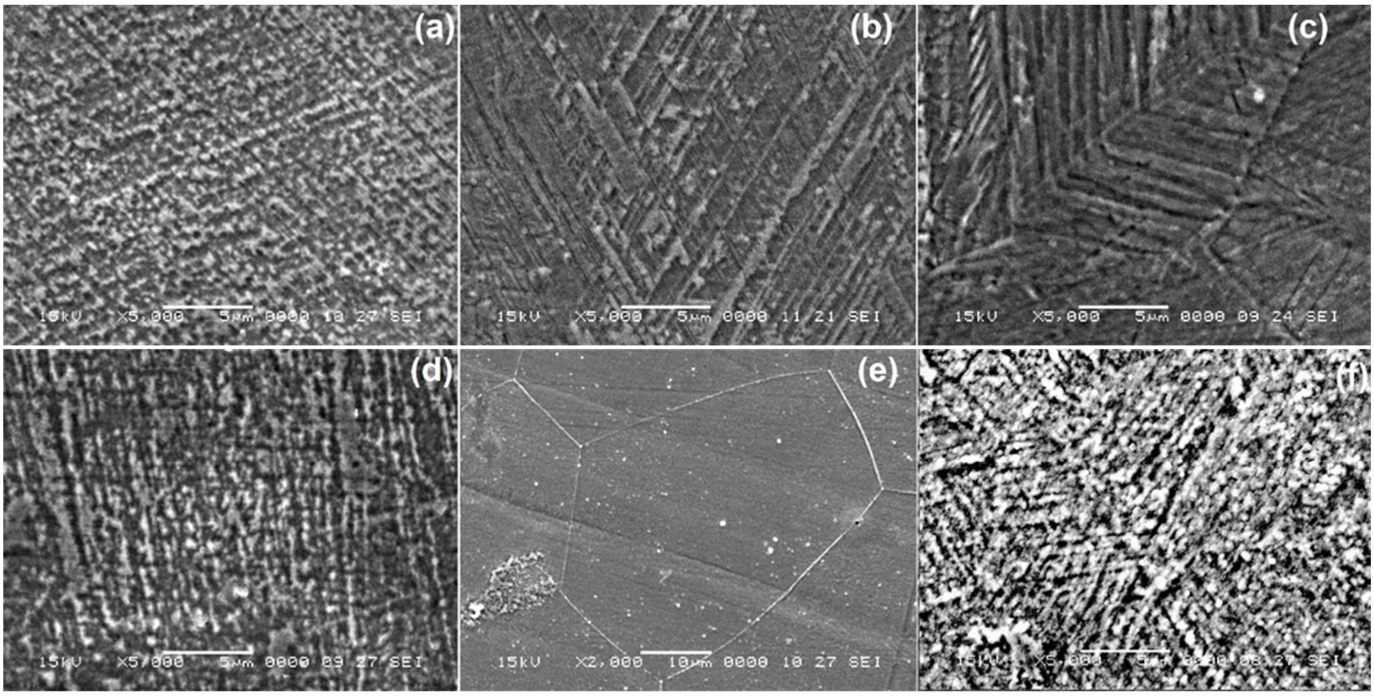

Figure 3. Typical SEM micrographs before DMA-SS-3PB: (**a**) in its initial hot-rolled state and at the specimens solution treated for: (**b**) 2 h; (**c**) 4 h; (**d**) 6 h; (**e**) 8 h; and (**f**) 10 h.

It is obvious that martensite plates can be observed neither in the initial hot-rolled state nor on the specimens that were solution-treated for 6, 8, and 10 h. Moreover, due to the precipitation emphasized in Figure 1a, the formation of martensite plates was completely hindered in Figure 3e. It can be concluded that thermally induced martensite formed only in the specimen solutions treated for 2 and 4 h.

After the application of DMA-SS-3PB, the occurrence of stress-induced martensite can be noticed even in the specimens in their initial hot-rolled state that were not subjected to solution treatment, as illustrated in Figure 4.

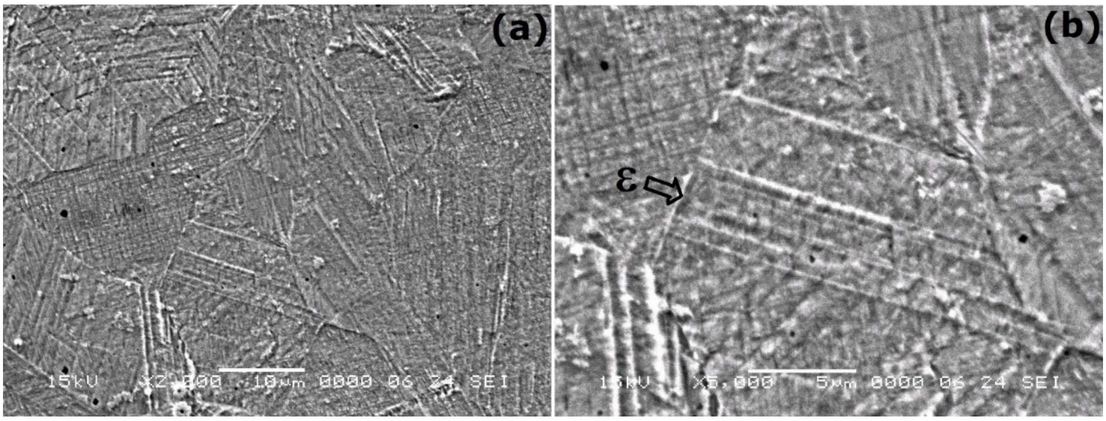

Figure 4. Typical SEM micrographs of a specimen in its initial hot-rolled state after DMA-SS-3PB: (**a**) general aspect; (**b**) detail of ε-hcp stress-induced martensite plates.

The plates shown in Figure 4b have submicronic widths and straight shapes, which are characteristic to ε-hcp martensite. By comparing the microstructure in Figure 3a, which corresponds to the specimen in initial hot-rolled state, with the microstructure shown in Figure 4, it is obvious that DMA-SS-3PB caused the occurrence of ε-hcp martensite plates.

The effects of DMA-SS-3PB on the structure of solution-treated specimens are emphasized in the typical SEM micrographs shown in Figure 5.

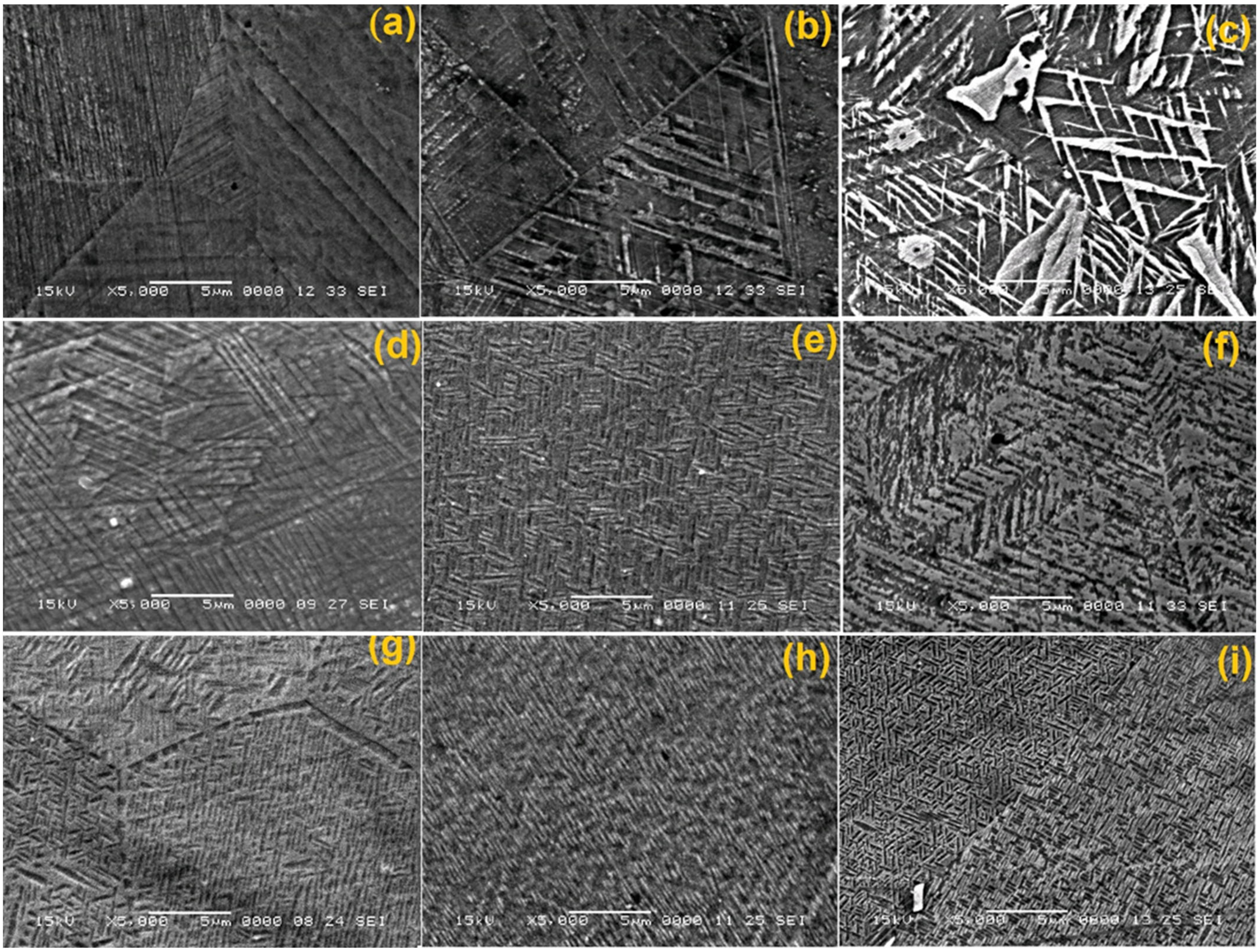

Figure 5. Typical SEM micrographs of solution-treated specimens after the application of DMA-SS-3PB: (**a**) 2 h–1 Hz; (**b**) 6 h–1 Hz; (**c**) 10 h–1 Hz; (**d**) 2 h–5 Hz; (**e**) 6 h–5 Hz; (**f**) 10 h–5 Hz; (**g**) 2 h–10 Hz; (**h**) 6 h–10 Hz; and (**i**) 10 h–10 Hz.

Two phenomena are noticeable from analyzing the micrographs in Figure 5:

(i) The grain size tends to increase with an increasing holding time due to coalescence enhancement as an effect of minimizing grain boundary energy at the solid–solid interface [28].

(ii) Stress-induced martensite plates become shorter with increasing the frequency of DMA-SS-3PB. Straight thin plates are visible only at the specimen solutions treated for 2 h (Figure 5a,d,g).

With an increasing holding time, the crystallites tend to become wider and preferably oriented. Specimen 10 h–10 Hz, from Figure 5i shows very short and precisely oriented submicronic particles, as detailed in Figure 6.

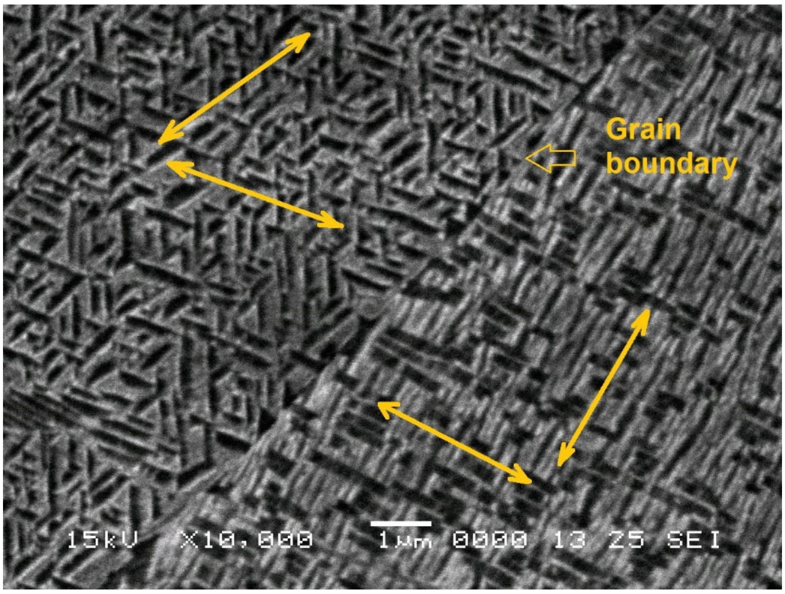

Figure 6. Detail of the SEM micrograph of specimen 10 h–10 Hz, from Figure 5i, emphasizing the crystallographic directions of the crystallites on both sides of a grain boundary.

It is obvious that the left-side particles are aligned along crystallographic directions tilted at approx. 60°, while those from the right side of the grain boundary make angles that are about 90°.

Considering that there were 5 DMA-SS-3PB cycles that each lasted for 14.9 min, it follows that the specimen 10 h–10 Hz was subjected to 14.9 min × 60 s × 10 oscillations/cycle × 5 cycles = 44,700 cycles. During this large number of cycles, martensite plates were stress-induced and fragmented to an average dimension of 0.2 × 1 μm. One can argue that for damping purposes, much larger numbers of cycles would be necessary within high-cycle fatigue testing. However, this is not the purpose of the present study.

3.4. XRD Investigations

XRD patterns were brought to the same scale and summarized in Figure 7.

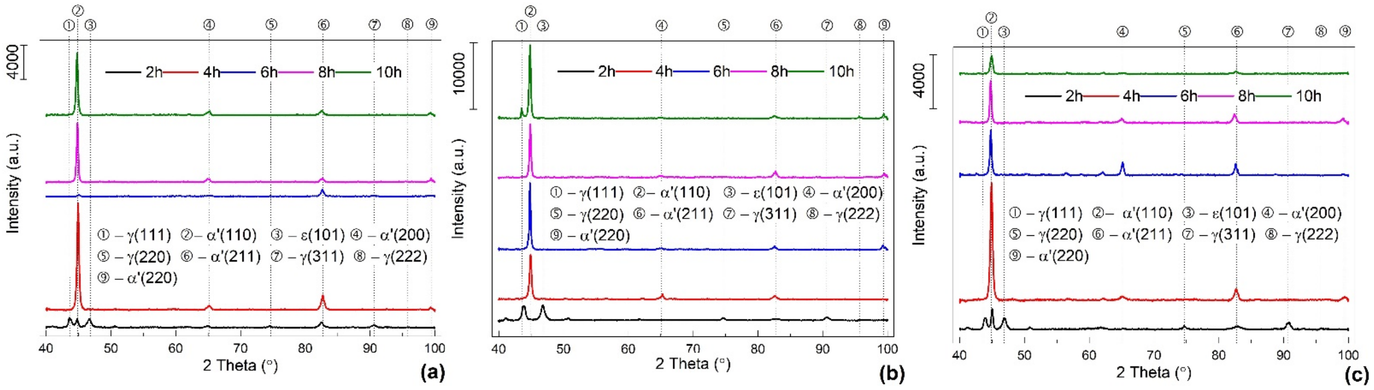

Figure 7. Typical XRD patterns of solution-treated specimens after the application of DMA-SS-3PB with different frequencies: (**a**) 1 Hz; (**b**) 5 Hz; and (**c**) 10 Hz.

By equalizing the XRD patterns, a more accurate qualitative analysis could be conducted with the single goal of emphasizing the occurrence of stress-induced martensite after DMA strain sweeps.

The crystallographic orientations (111), (220), and (311) are known for enhancing the stress-induced martensite reversion to austenite upon mechanical unloading [29], and for this reason, they are absent on the XRD patterns of the large majority of the specimens. Due to the accumulation of a large amount of dynamical deformation during the five DMA-SS-3PB cycles applied to each specimen, the formation of α′-bcc martensite was favored. In order to evaluate its unit cell deformation, the experimental values of its parameter, a_{exp}, were calculated. Bragg's Law was used to determine lattice spacings d_{110} (based on Cu wavelength λ_{Cu} = 0.1540598 nm and the experimental values of $2\theta/2$ angles). Then, a_{exp} values were calculated based on lattice spacings and experimental Miller indices [30].

Finally, the experimental value, a_{exp}, was subtracted from the theoretical one, a_{theor} = 0.3592 nm, given by the JCPDS files of 00-034-0396 crystallographic database. The variations of $\Delta a = a_{exp} - a_{theor}$, as a function of the holding time and DMA-SS-3PB frequency, are shown in Figure 8.

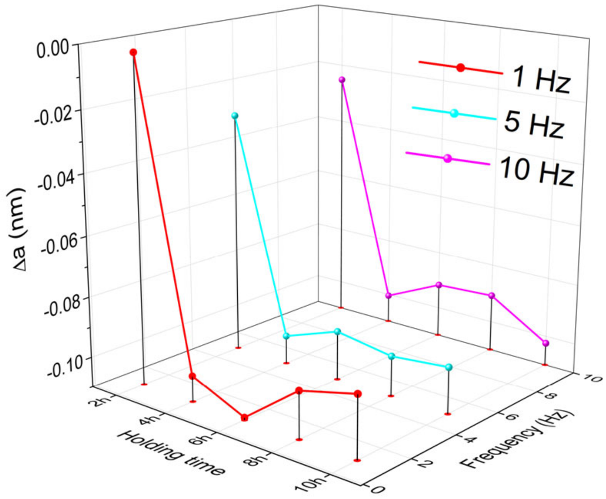

Figure 8. Variation of the unit cell deformation of α′-bcc martensite as a function of holding time and DMA-SS-3PB frequency, according to the XRD patterns from Figure 7.

It is obvious that, for each of the three DMA-SS-3PB frequencies, the unit cell of α′-bcc martensite was compressed by as much as a third of its initial value. It follows that the martensite is no longer cubic but becomes tetragonal after dynamical bending.

3.5. AFM Observations

For a better look at the changes induced by the holding time and strain sweep frequency, AFM observations were performed. Figure 9 shows the representative AFM micrographs of the specimens that were subjected to the shortest and longest holding times.

The AFM micrographs reveal martensite plate refinement with the increased holding time and the DMA-SS-3PB frequency. For the quantitative evaluation of the effects of the extreme values of the holding time and the deformation frequency on martensite plate dimensions, systematic measurements were performed. For this purpose, five characteristic groups ($i = 1 \div 5$) of martensite plates and five parallel plates ($j = 1 \div 5$) within each group were selected. Along each plate, the width and height of five equidistant profiles were measured, and the average values of the width (w_{ij}) and height (h_{ij}) were calculated for each plate along with the corresponding standard deviations. The results are listed in Table 1.

Table 1. Experimental values of martensite plate widths and heights (nm).

Specimen	Plate Group No.	Plate No.	Dimension	Average Value	Standard Deviation	Specimen	Plate Group No.	Plate No.	Dimension	Average Value	Standard Deviation
2 h–1 Hz	1	1	w_{11}	16,244	770.2	2 h–10 Hz	1	1	w_{11}	791	89.3
			h_{11}	8639	675.8				h_{11}	571	147
		2	w_{12}	19,184	582.9			2	w_{12}	626	66.1
			h_{12}	11,404	463.4				h_{12}	458	106.3
		3	w_{13}	7376	800.7			3	w_{13}	3037	353.6
			h_{13}	4174	585				h_{13}	1803	369.6
		4	w_{14}	6797	2997.5			4	w_{14}	446	46.4
			h_{14}	4856	699.6				h_{14}	278	19.4
		5	w_{15}	5538	470.7			5	w_{15}	597	120.8
			h_{15}	3921	344.2				h_{15}	264	74.6
	2	1	w_{21}	4795	431.4		2	1	w_{21}	686	140.2
			h_{21}	2798	219.3				h_{21}	404	133.7
		2	w_{22}	4776	128.3			2	w_{22}	687	111.4
			h_{22}	2972	216.2				h_{22}	437	107.4
		3	w_{23}	4961	350.8			3	w_{23}	837	123.9
			h_{23}	3478	455.2				h_{23}	462	50.1
		4	w_{24}	2225	258.6			4	w_{24}	8173	1257.5
			h_{24}	1267	275.6				h_{24}	6040	898.9
		5	w_{25}	11,878	794.5			5	w_{25}	13,300	645.9
			h_{25}	7030	641.9				h_{25}	7539	852.5
	3	1	w_{31}	14,440	460.4		3	1	w_{31}	10,412	820.7
			h_{31}	8279	721				h_{31}	6912	603.3
		2	w_{32}	6519	435.5			2	w_{32}	11,463	2182.3
			h_{32}	4303	571.7				h_{32}	6475	658.2
		3	w_{33}	2302	345.1			3	w_{33}	669	247.7
			h_{33}	1696	102.4				h_{33}	432	168.6
		4	w_{34}	6403	510.7			4	w_{34}	661	122.9
			h_{34}	3960	89				h_{34}	288	72.4
		5	w_{35}	7784	306.6			5	w_{35}	544	69.9
			h_{35}	3852	262.2				h_{35}	369	55.6

Table 1. *Cont.*

Specimen	Plate Group No.	Plate No.	Dimension	Average Value	Standard Deviation	Specimen	Plate Group No.	Plate No.	Dimension	Average Value	Standard Deviation
	4	1	w_{41}	9855	534.8		4	1	w_{41}	738	243.7
			h_{41}	5458	648.7				h_{41}	475	184.1
		2	w_{42}	4131	272			2	w_{42}	606	187.7
			h_{42}	3237	287.3				h_{42}	366	127.4
		3	w_{43}	3764	420.4			3	w_{43}	563	194.1
			h_{43}	4041	949.4				h_{43}	335	193.1
		4	w_{44}	6286	421.4			4	w_{44}	397	54.4
			h_{44}	3700	372.3				h_{44}	237	47.6
		5	w_{45}	10,320	264			5	w_{45}	328	86.4
			h_{45}	5889	254				h_{45}	264	77.3
	5	1	w_{51}	7146	674.9		5	1	w_{51}	399	84.6
			h_{51}	394	422.2				h_{51}	218	22.9
		2	w_{52}	4085	240.7			2	w_{52}	340	68.3
			h_{52}	3456	188.6				h_{52}	221	27.6
		3	w_{53}	4066	531.2			3	w_{53}	432	60.5
			h_{53}	2574	1312.5				h_{53}	254	64
		4	w_{54}	2361	206.6			4	w_{54}	448	57.7
			h_{54}	1891	160.5				h_{54}	230	39.4
		5	w_{55}	3631	318.7			5	w_{55}	660	40.5
			h_{55}	2245	251.3				h_{55}	311	47.3
10 h–1 Hz	1	1	w_{11}	6355	1265.5	10 h–10 Hz	1	1	w_{11}	848	128.6
			h_{11}	4225	166.5				h_{11}	505	106.4
		2	w_{12}	3896	440.7			2	w_{12}	939	73
			h_{12}	2574	181.8				h_{12}	454	49
		3	w_{13}	2999	516.8			3	w_{13}	713	96.6
			h_{13}	1608	169.6				h_{13}	937	61
		4	w_{14}	2460	320.9			4	w_{14}	744	66
			h_{14}	1732	225.8				h_{14}	476	24.2
		5	w_{15}	2529	480.5			5	w_{15}	859	42.7
			h_{15}	1432	311.4				h_{15}	480	28.7

Table 1. *Cont.*

Specimen	Plate Group No.	Plate No.	Dimension	Average Value	Standard Deviation	Specimen	Plate Group No.	Plate No.	Dimension	Average Value	Standard Deviation
	2	1	w_{21}	3665	361.4		2	1	w_{21}	673	13.2
			h_{21}	2801	70.8				h_{21}	381	53.2
		2	w_{22}	3056	210.1			2	w_{22}	658	82.5
			h_{22}	2273	187.9				h_{22}	391	32
		3	w_{23}	1059	55.8			3	w_{23}	737	82
			h_{23}	526	54				h_{23}	402	40.1
		4	w_{24}	983	57.5			4	w_{24}	999	127.2
			h_{24}	501	66.8				h_{24}	516	85.2
		5	w_{25}	763	81.9			5	w_{25}	842	100.3
			h_{25}	433	49.7				h_{25}	485	65.6
	3	1	w_{31}	620	185.9		3	1	w_{31}	695	40.5
			h_{31}	380	118.5				h_{31}	429	28.8
		2	w_{32}	694	74.4			2	w_{32}	694	66
			h_{32}	416	25.5				h_{32}	430	30.4
		3	w_{33}	619	88.9			3	w_{33}	808	80.5
			h_{33}	361	47				h_{33}	527	101.9
		4	w_{34}	740	72			4	w_{34}	782	22.6
			h_{34}	381	39.5				h_{34}	417	28.5
		5	w_{35}	866	80.6			5	w_{35}	664	140.1
			h_{35}	471	43.8				h_{35}	327	73.3
	4	1	w_{41}	791	49.5		4	1	w_{41}	327	24.8
			h_{41}	428	50				h_{41}	188	24.7
		2	w_{42}	936	48.7			2	w_{42}	350	37.5
			h_{42}	466	41.5				h_{42}	194	22.4
		3	w_{43}	2032	110.2			3	w_{43}	824	210
			h_{43}	1044	57				h_{43}	387	65.9
		4	w_{44}	798	166.3			4	w_{44}	706	31.1
			h_{44}	533	146.8				h_{44}	336	41.5
		5	w_{45}	1779	150.6			5	w_{45}	707	57.1
			h_{45}	911	90.1				h_{45}	345	42.5

Table 1. *Cont.*

Specimen	Plate Group No.	Plate No.	Dimension	Average Value	Standard Deviation	Specimen	Plate Group No.	Plate No.	Dimension	Average Value	Standard Deviation
	5	1	w_{51}	1235	51.4		5	1	w_{51}	326	67.2
			h_{51}	775	63.7				h_{51}	144	20
		2	w_{52}	1118	169.6			2	w_{52}	311	52.1
			h_{52}	687	61.2				h_{52}	188	42.3
		3	w_{53}	948	94.3			3	w_{53}	714	34.9
			h_{53}	524	37.4				h_{53}	339	20.7
		4	w_{54}	884	50.1			4	w_{54}	870	54.6
			h_{54}	518	59.3				h_{54}	395	57.7
		5	w_{55}	665	65.8			5	w_{55}	340	74.4
			h_{55}	406	23.9				h_{55}	177	40

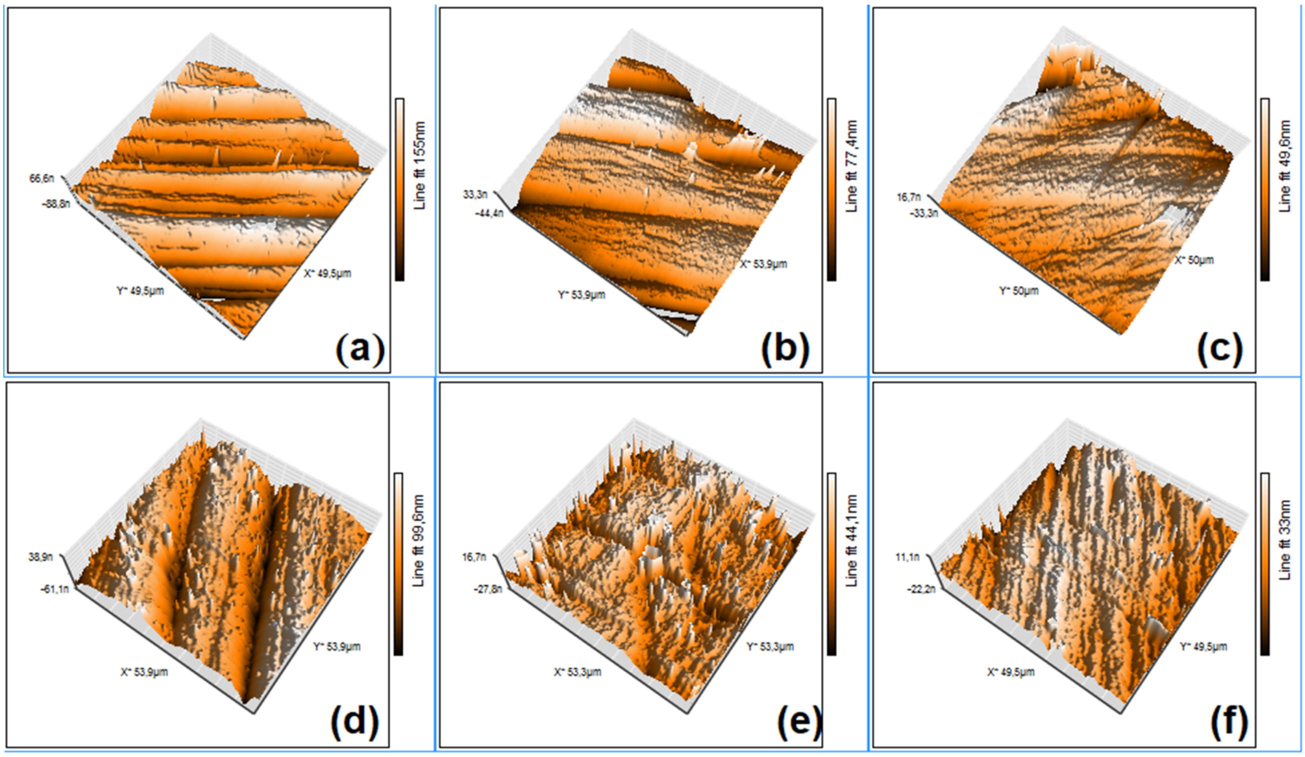

Figure 9. Typical AFM micrographs of solution-treated specimens, after the application of DMA-SS-3PB: (**a**) 2 h–1 Hz; (**b**) 2 h–5 Hz; (**c**) 2 h–10 Hz; (**d**) 10 h–1 Hz; (**e**) 10 h–5 Hz; and (**f**) 10 h–10 Hz.

By averaging the values listed in Table 1, the mean heights and widths of the martensite plates can be determined for the four specimens that were processed under extreme holding time and deformation frequency conditions, as summarized in Table 2.

Table 2. Mean values of martensite widths (w_{mean}) and heights (h_{mean}) determined from Table 1 (nm).

Specimen	2 h–1 Hz	2 h–10 Hz	10 h–1 Hz	10 h–10 Hz
w_{mean}	6913	2298	1664	659
h_{mean}	4119	1417	1037	382

These values are in good agreement with the resultsFi obtained from SEM micrographs, and they demonstrate that the increase in both the holding time and deformation frequency caused the refinement of martensite plates. Nevertheless, the increase in the holding time from 2 to 10 h caused a decrease in the martensite plate width between 4.15 and 3.49 times and a decrease in their height between 3.97 and 3.71 times. Conversely, a frequency increase from 1 to 10 Hz caused plate width decreases of between 3 and 2.5 times and plate height decreases of between 2.9 and 2.7 times. These results prove that a holding time increase from 2 to 10 h is more effective than a deformation frequency increase from 1 to 10 Hz, from the point of view of martensite plate refinement.

4. Discussion

Finally, before ending the discussion of the above results, one should also consider the unique character of the martensite plates, which are stress-induced in Fe-Mn-Si-based SMAs during dynamic loading. It has been demonstrated that these SMAs experience the transformation of the martensite plate variants that reversibly change from tension-induced to compression-induced [31]. It can be assumed that this phenomenon also occurs during DMA strain sweep, when the specimens are alternatively bent by the analyzer's pushrod.

It has been argued that stress-induced martensite plates should not intersect each other, and for this reason, it is recommended that they have small dimensions and a reduced number of crystallographic orientations [5]. Or this is exactly what the combination of 10 h of holding and a 10 Hz strain sweep has achieved, as pointed out by Figure 6 and Table 2.

The storage modulus reinforcement of the Fe-28Mn-6Si-5Cr SMA under this study, as an effect of dynamic strain sweep, is more desirable from the point of view of shape recovery stresses than from the point of view of vibration mitigation.

5. Conclusions

By summarizing the results of the investigations performed by DSC, DMA, SEM, XRD, and AFM, the following conclusions can be drawn concerning the effects of the solution treatment holding time and RT dynamical deformation frequency:

1. A precipitation phenomenon was identified by DSC in the specimens that were solution-treated for 8 and 10 h;
2. Dynamical deformations by RT strain sweeps caused work hardening and a general increase in the storage modulus;
3. At the precipitate-free specimens, which were solution-treated for 2 and 4 h, internal friction ranged between 0.1 and 0.2;
4. Neither in the initial hot-rolled specimens nor in the specimens that were solution-treated between 6 and 10 h, the martensite plates were not visible on SEM micrographs;
5. The application of RT strain sweeps caused the occurrence of stress-induced martensite or the fragmentation of the thermally induced one;
6. In solution-treated specimens, the increase in the holding time (from 2 to 10 h) was more effective than the increase in the deformation frequency (from 1 to 10 Hz) in the refinement of martensite plates;
7. After 10 h of holding at 1050 °C and the strain sweep application at a frequency of 10 Hz, the martensite plates reached the minimum mean values of their width (659 nm) and height (382 nm) and became preferably oriented;
8. The recorded XRD patterns indicated that after the dynamic deformation, most of the microstructure comprises mostly α'-bcc martensite, which was due to the high amount of dynamical deformation induced by the RT strain sweep;
9. A holding time increase from 2 to 10 h enhanced the compression of the parameter of the cubic unit cell by approx. 30%, which changed the crystallization system from cubic to tetragonal-centered cubic.
10. A new mechanical treatment has been introduced for Fe-Mn-Si-based SMAs, based on RT isothermal dynamic bending, which is able to reinforce the storage modulus and refine the martensitic structure.

Supplementary Materials: The following supporting information can be downloaded at: https://www.mdpi.com/article/10.3390/nano13071250/s1, Figure S1: The gradual change in the shape of manufactured specimens.

Author Contributions: Conceptualization, M.P. and L.-G.B.; methodology, L.-G.B.; software, M.P. and B.P.; validation, B.P., N.-M.L. and N.C.; formal analysis, M.P.; investigation, F.P., B.P., B.I. and N.C.; resources, M.P. and G.K.; data curation, N.-M.L., B.I. and G.K.; writing—original draft preparation, L.-G.B.; writing—review and editing, L.-G.B.; visualization, B.P.; supervision, N.C. and N.-M.L.; project administration, M.P.; funding acquisition, L.-G.B. All authors have read and agreed to the published version of the manuscript.

Funding: This research received no external funding.

Data Availability Statement: Not applicable.

Conflicts of Interest: The authors declare no conflict of interest. The funders had no role in the design of the study; in the collection, analyses, or interpretation of data; in the writing of the manuscript, or in the decision to publish the results.

References

1. Maki, T. Ferrous shape memory alloys. In *Shape Memory Materials*; Otsuka, K., Wayman, C.M., Eds.; University Press: Cambridge, UK, 1998; pp. 117–132.
2. Cao, B.; Iwamoto, T. A new method to measure volume resistivity during tension for strain sensitivity deformation and transformation behaviour of $Fe_{28}Mn_6Si_5Cr$ shape memory alloy. *Int. J. Mech. Sci.* **2018**, *156–157*, 445–454. [CrossRef]
3. Dong, Z.Z.; Kajiwara, S.; Kikuchi, T.; Sawaguchi, T. Effect of pre-deformation at room temperature on shape memory properties of stainless type Fe–15Mn–5Si–9Cr–5Ni–(0.5–1.5)NbC alloys. *Acta Mater.* **2005**, *53*, 5009–5018. [CrossRef]
4. Sato, A.; Chishima, E.; Soma, K.; Mori, T. Shape memory effect in $\gamma\leftrightarrow\varepsilon$ transformation in Fe-30Mn-1Si alloy single crystals. *Acta Metall. Mater.* **1982**, *30*, 1177–1183. [CrossRef]
5. Kajiwara, S. Characteristic features of shape memory effect and related transformation behavior in Fe-based alloys. *Mat. Sci. Eng. A* **1999**, *273–275*, 67–88. [CrossRef]
6. Arruda, G.J.; Buono, V.T.L.; Andrade, M.S. The influence of deformation on the microstructure and transformation temperatures of Fe–Mn–Si–Cr–Ni shape memory alloys. *Mater. Sci. Eng. A* **1999**, *273–275*, 528–532. [CrossRef]
7. Otsuka, H.; Yamada, H.; Maruyama, T.; Tanahashi, H.; Matsuda, S.; Murakami, M. Effects of alloying additions on Fe-Mn-Si shape memory alloys. *ISIJ Int.* **1990**, *30*, 675–679. [CrossRef]
8. Kajiwara, S.; Baruj, A.; Kikuchi, T.; Shinya, N. Low-cost high-quality Fe-based shape memory alloys suitable for pipe joints. In *Smart Structures and Materials*; Lagoudas, D.C., Ed.; SPIE: Bellingham, WA, USA, 2003; Volume 5053, pp. 250–261.
9. Farjami, S.; Hiraga, K.; Kubo, H. Shape memory effect and crystallographic investigation in VN containing Fe-Mn-Si-Cr alloys. *Mater. Trans.* **2005**, *55*, 930–935. [CrossRef]
10. Maruyama, T.; Kurita, T.; Kozaki, S.; Andou, K.; Farjami, S.; Kubo, H. Innovation in producing crane rail fishplate using Fe-Mn-Si-Cr based shape memory alloy. *Mater. Sci. Technol.* **2008**, *25*, 908–912. [CrossRef]
11. Sawaguchi, T.; Kikuchi, T.; Ogawa, K.; Yin, F.X.; Kajiwara, S.; Kushibe, A.; Ogawa, T. Internal Friction of Fe-Mn-Si-Based Shape Memory Alloys Containing Nb and C and Their Application as a Seismic Damping Material. *Key Eng. Mater.* **2006**, *319*, 53–58. [CrossRef]
12. Paleu, V.; Gurău, G.; Comăneci, R.I.; Sampath, V.; Gurău, C.; Bujoreanu, L.G. A new application of Fe-28Mn-6Si-5Cr (mass%) shape memory alloy, for self-adjustable axial preloading of ball bearings. *Smart Mater. Struct.* **2018**, *27*, 075026. [CrossRef]
13. Sawaguchi, T.; Sahu, P.; Kikuchi, T.; Ogawa, K.; Kajiwara, S.; Kushibe, A.; Higashino, M.; Ogawa, T. Vibration mitigation by the reversible fcc/hcp martensitic transformation during cyclic tension–compression loading of an Fe–Mn–Si-based shape memory alloy. *Scripta Mater.* **2006**, *55*, 1885–1890. [CrossRef]
14. Bidaux, J.-E.; Schaller, R.; Benoit, W. Study of hcp-fcc phase transition in Cobalt by acoustic measurements. *Acta Metall.* **1989**, *37*, 803–811. [CrossRef]
15. De, A.K.; Cabanas, N.; De Cooman, B.C. Fcc-hcp Transformation-Related Internal Friction in Fe-Mn Alloys. *Int. J. Mater. Res.* **2002**, *93*, 228–235. [CrossRef]
16. Van Humbeeck, J.; Stoiber, J.; Delaey, L.; Gotthardt, R. The high damping capacity of shape-memory alloys. *Int. J. Mater. Res.* **1995**, *86*, 176–183. [CrossRef]
17. Wetton, R.E. Thermomechanical methods. In *Handbook of Thermal Analysis and Calorimetry*; Brown, M.E., Ed.; Principles and Practice; Elsevier Science: Amsterdam, The Neverlands, 1998; Volume 1, pp. 363–399.
18. Bulbuc, V.; Pricop, B.; Maxim, F.; Popa, M.; Cimpoesu, N.; Bujoreanu, L.G. Influence of dynamic three point bending on the work hardening capacity of T105Mn120 manganese steel. *J. Mater. Eng. Perform.* **2018**, *27*, 6127–6135. [CrossRef]
19. Bulbuc, V.; Pricop, B.; Maxim, F.; Popa, M.; Cimpoesu, N.; Bujoreanu, L.-G. Variation of damping behaviour of T105Mn120 castings, used for railway safety systems, as an effect of extreme loading conditions. *Mater. Today Proc.* **2019**, *19*, 949–955. [CrossRef]
20. Chung, C.Y.; Chen, S.; Hsu, T.Y. Thermomechanical training behavior and its dynamic mechanical analysis in an Fe-Mn-Si shape memory alloy. *Mater. Char.* **1996**, *37*, 227–236. [CrossRef]
21. Dong, Z.Z.; Sawaguchi, T.; Kikuchi, T.; Yin, F.; Ogawa, K.; Sahu, P.; Kajiwara, S. Internal friction study on fcc/hcp martensitic transformations in thermomechanically treated Fe–28Mn–6Si–5Cr–0.53Nb–0.06C (mass%) alloys. *Mater. Sci. Eng. A.* **2006**, *552*, 505–508. [CrossRef]
22. Popa, M.; Pricop, B.; Mihalache, E.; Bujoreanu, L.G. Storage modulus and internal friction variations in a Fe-28Mn-6Si-5Cr (mass. %) shape memory alloy analyzed by three point-bending DMA. *IOP Conf. Series Mater. Sci. Eng.* **2017**, *227*, 012099. [CrossRef]
23. Popa, M.; Lohan, N.-M.; Popa, F.; Pricop, B.; Bujoreanu, L.-G. Holding-temperature effects on thermally and stress induced martensitic transformations in an FeMnSiCr SMA. *Mater. Today: Proc.* **2019**, *19*, 956–962. [CrossRef]
24. Tasaki, W.; Sawaguchi, T.; Tsuchiya, K. EBSD analysis of dual γ/ε phase microstructures in tensile-deformed Fe-Mn-Si shape memory alloy. *J. Alloy. Compd.* **2019**, *797*, 529–536. [CrossRef]
25. Suru, M.G.; Bujoreanu, L.-G. Comparative topographic study of surface micro-relief of primary martensite plates in shape memory alloys with different crystalline structures. *Mat.-Wiss. U. Werkstofftech.* **2012**, *53*, 973–978. [CrossRef]
26. Zlá, S.; Smetana, B.; Žaludová, M.; Dobrovská, J.; Vodárek, V.; Konečná, K.; Matějka, V.; Francová, H. Determination of thermophysical properties of high temperature alloy IN713LC by thermal analysis. *J. Therm. Anal. Calorim.* **2012**, *110*, 211–219. [CrossRef]

27. Sawaguchi, T.; Bujoreanu, L.G.; Kikuchi, T.; Ogawa, K.; Yin, F. Effects of Nb and C in solution and in NbC form on the transformation-related internal friction of Fe–17Mn (mass%) alloys. *ISIJ Int.* **2008**, *58*, 99–106. [CrossRef]
28. Han, C.; Jiang, P.; Geng, S.; Gao, S.; Mi, G.; Wang, C. Multiphase-field simulation of grain coalescence behavior and its effectson solidification cracking susceptibility during welding of Al-Cu alloys. *Mater. Design* **2021**, *211*, 1101561. [CrossRef]
29. Yang, Y.; Leinenbach, C.; Shahverdi, M. Simulation and experimental characterization of VC precipitation and recovery stress formation in an FeMnSi-based shape memory alloy. *J. Alloy. Comp.* **2023**, *950*, 168856. [CrossRef]
30. Cullity, B.D. *Elements of X-ray Diffraction*; Addison-Wesley Publishing Company: Boston, MA, USA, 1956; pp. 37–52.
31. Sawaguchi, T.; Bujoreanu, L.G.; Kikuchi, T.; Ogawa, K.; Koyama, M.; Murakami, M. Mechanism of reversible transformation-induced plasticity of Fe–Mn–Si shape memory alloys. *Scripta Mater.* **2008**, *59*, 826–829. [CrossRef]